



# Low-Energy Au Ion Beam Implantation in the Optical, Structural, and Surface Properties of RF-Sputtered WO<sub>3</sub> Thin Films

Deepika<sup>1</sup> · Rajesh Kumar<sup>1</sup>

Received: 12 March 2024 / Accepted: 2 May 2024 / Published online: 30 May 2024  
© The Minerals, Metals & Materials Society 2024

## Abstract

WO<sub>3</sub> is considered to be significant for diverse applications such as gas sensing, photocatalysts, and photovoltaic devices because of its optical wide band gap. Ion beam treatment of various metal oxides produces defects that modify various properties such as topographical, structural, and optical characteristics of the metal oxides. When the energetic ion pass through the target materials, it causes two kinds of energy losses, i.e., nuclear and electronic energy loss. In low-energy ion beam treatment of thin films, nuclear energy loss dominates over electronic energy loss. In our current study, thin films of tungsten oxide were grown on substrates of glass and silicon by the RF-sputtering method. The sputtered WO<sub>3</sub> thin films were exposed to an ion beam of Au ions with an energy of 80 keV at various fluences of 5E14 ions/cm<sup>2</sup>, 1E15 ions/cm<sup>2</sup>, and 5E15 ions/cm<sup>2</sup>. Atomic force microscopy (AFM) shows that, after implantation, enhancement in grain size was observed from 49.5 nm to 56.6 nm. The optical study displays the alteration in the energy band gap of ion-implanted WO<sub>3</sub> thin films from 2.75 eV to 2.99 eV. From Raman spectroscopy, the phase observed is monoclinic for virgin and implanted samples. PL spectroscopy of virgin and ion beam-implanted WO<sub>3</sub> thin films shows emission spectra at the wavelength of 580 nm at an excitation wavelength of 420 nm. X-ray photoelectron spectroscopy shows the appearance of tungsten and oxygen atoms and shows the electronic structure variation after Au ion beam implantation.

**Keywords** Thin films · RF-sputtering · ion beam · AFM · Raman · UV-vis · XRD · XPS

## Introduction

In the last few years, much focus has been paid to metal oxide nanoparticles or nitride micro- and nanostructured materials due to their physicochemical, structural, optical, and corrosion properties, which show vast potential applications.<sup>1–3</sup> Metal oxide micro- and nanostructures have been used in several applications, such as solar energy, photocatalysis, wastewater treatment, and microelectronics, because of their unique structural and morphological properties.<sup>4–7</sup> Of numerous metal oxides, tungsten oxide (WO<sub>3</sub>) is an auspicious material utilized by the scientific community because it is cost-effective, and has a huge band gap and

high solubility in aqueous solutions. Tungsten oxide is considered an *n*-type semiconductor having an empty perovskite structure formed by WO<sub>3</sub> nanostructures.<sup>8,9</sup> Tungsten oxide possesses various structures including monoclinic (17–330 °C), orthorhombic (330–740 °C), and tetragonal (> 740 °C).<sup>10</sup> The most commonly used structure of WO<sub>3</sub> is the monoclinic structure.<sup>8</sup> WO<sub>3</sub> thin films have been extensively used in discrete application fields like gas-sensing,<sup>11</sup> photoelectrochemical,<sup>12</sup> electrochromic devices,<sup>13,14</sup> and optoelectronic devices.<sup>15</sup> Tungsten oxide has a high melting point and it has better catalytic characteristics for hydro-generation reactions.<sup>16–18</sup> Tungsten oxide has been used for the decomposition of pollutants and dyes because of its redox potential.<sup>18–20</sup> WO<sub>3</sub> nanomaterial has been fabricated in different structures and different phases comprising nanoplates, nanotubes, nanoleaves, nanorods, nanoflakes, etc., and has been synthesized by various techniques, such as solvothermal synthesis,<sup>21</sup> metal–organic chemical vapor deposition,<sup>22</sup> hydrothermal processes,<sup>23</sup> sol–gel technique,<sup>24,25</sup> magnetron sputtering, spray pyrolysis,<sup>26</sup> vacuum evaporation,<sup>27</sup> electron

✉ Rajesh Kumar  
kumarrpi@gmail.com

<sup>1</sup> University School of Basic and Applied Sciences, Guru Gobind Singh Indraprastha University, New Delhi 110078, India

beam irradiation,<sup>28</sup> liquid-phase depositions,<sup>29</sup> flame-based solid evaporation,<sup>30</sup> electrical arc discharge method<sup>31</sup> and microwave synthesis.<sup>32</sup> Of all these deposition approaches, the sputtering approach is the best method for producing homogenous arrangements and stoichiometrics of WO<sub>3</sub> thin films.<sup>33,34</sup> Yousif et al.<sup>35</sup> prepared WO<sub>3</sub> thin films by pulsed laser deposition and found the alteration in structural and optical characteristics of WO<sub>3</sub> thin films with treatment of heat. Haung et al.<sup>36</sup> fabricated WO<sub>3</sub> thin films by a hydrothermal procedure and studied the temperature variation of the structure and photochromic traits of WO<sub>3</sub> powder. Rathika et al.<sup>37</sup> synthesized WO<sub>3</sub> thin film by spray pyrolysis and studied modifications in the optical, structural, and morphological properties of WO<sub>3</sub> thin films.

Hence, by modification in tungsten-based materials, they can be used in various applications. Irradiation with an ion beam is a significant approach for alteration in the material at the nanoscale level. Recent research shows that ion beam irradiation modifies the characteristics of nanomaterials with high fidelity.<sup>38</sup> When the energetic ions enter the targeted material, energy is lost in two ways: electronic or nuclear energy loss. When the incident ion collides inelastically with the electron cloud of the targeted material, this causes a loss of electronic energy, while nuclear energy loss arises when the ions are incident with energy from keVs to 2 MeV and interact elastically with the targeted material.<sup>39,40</sup> Electronic energy losses (Se) are overcome at high energy (> 1 MeV/nucleon) and nuclear energy losses (Sn) are found at low energy (~ keV/nucleon). In the elastic collision, nuclear energy loss was dominated by electronic energy losses which produced point defects, development of dislocation loops, and a cluster of defects in the targeted material.<sup>41–44</sup> The surface morphology alteration of the sample by irradiation with an ion beam has been used for device applications.<sup>45–47</sup> Various research groups have shown modifications in the optical, structural, and morphological properties of the sample after ion beam irradiation. Sivakumar et al. observed the effect of an ion beam on the thin film of WO<sub>3</sub> irradiated by an N<sup>+</sup> ion beam with MeV energy, and found devaluation in the optical band gap of WO<sub>3</sub> virgin and ion-irradiated thin films.<sup>48</sup> Sharma et al.<sup>49</sup> irradiated thin films of WO<sub>3</sub> by 100 MeV Ni<sup>7+</sup> ions with varying sputtering pressure from 10 to 50 mTorr, and found that the grain size is enhanced and the band gap decreased after ion beam irradiation. Rathika et al.<sup>37</sup> irradiated WO<sub>3</sub> thin film by Ag<sup>15+</sup> ions with the energy of 200 MeV with varying fluences (5 × 10<sup>11</sup>, 1 × 10<sup>12</sup>, 5 × 10<sup>12</sup>, and 1 × 10<sup>13</sup> ions/cm<sup>2</sup>) and they found that the band gap decreased from 3.45 nm to 3.32 nm and surface modifications were observed after exposure to ion beams. Kumar et al.<sup>50</sup> grew thin films of TiO<sub>2</sub> by the RF-sputtering method and thin films were irradiated with an ion beam with 800 keV with distinct fluences (1E15 ions/cm<sup>2</sup> to

1E17 ions/cm<sup>2</sup>). They observed that the crystal size reduced from 42.09 to 27.36 nm after ion beam irradiation.

Figure 1 shows a schematic of our work. The tungsten oxide thin films were synthesized by RF-sputtering and were then exposed to ion beam irradiation with 80 keV energy and an Au ion beam at different fluences (5E14, 1E15, and 5E15) before we analyzed the variation in different properties, such as optical, morphological, and structural, of WO<sub>3</sub> thin films. Then, various characterizations such as X-ray diffraction (XRD), atomic force microscopy (AFM), UV-visible, Raman spectroscopy, photoluminescence (PL) spectroscopy, and X-ray photoelectron spectroscopy (XPS) were carried out.

## Experimental

### Thin Film Preparation

WO<sub>3</sub> powder was commercially purchased from Sigma Aldrich with 99.99% purity. Then, the target was formed by using a 2-inch (c. 5-cm) die with 6-tonne pressure. Thin films of WO<sub>3</sub> were grown at MNIT Jaipur by the RF sputtering method because it enables more economical deposition onto substrates of large areas. The thin films were deposited at room temperature by optimizing the parameter with the power of 100 W, working pressure of 3 × 10<sup>-2</sup> with 10–12 rpm rotation, and the distance of the target from the substrate of 8 cm. After deposition of the WO<sub>3</sub> thin films, they were annealed at 550°C for 24 h.

### Ion Beam Irradiation

After the deposition of the WO<sub>3</sub> thin films, they were irradiated by an Au ion beam with 80 keV energy at varying fluences of 5E14 ions/cm<sup>2</sup>, 1E15 ions/cm<sup>2</sup>, and 5E15 ions/cm<sup>2</sup>. The WO<sub>3</sub> thin films were irradiated by a Pelletron accelerator tandem (15UD) at the Inter-University Accelerator Center, New Delhi. James F. Ziegler and Biersack developed the SRIM software and they also gave us Monte Carlo simulation software known as TRIM.<sup>51</sup> This investigates various parameters such as phonon generation, ionization, losses of energy, and range of the target. SRIM/TRIM simulation software was used for observing the damage originating in the material irradiated with an ion beam. Electronic energy and nuclear energy loss with an 80-keV ion beam are illustrated in Fig. 2. The ionic path, atom displacement, and target ionization of the thin films were calculated by TRIM-2013 simulation software. The ion range was observed to be 20.5 nm and the straggling range was found to be 8.6 nm, as displayed in Fig. 3a–d. In an ion beam irradiation with low energy, nuclear energy loss is greater than the electronic

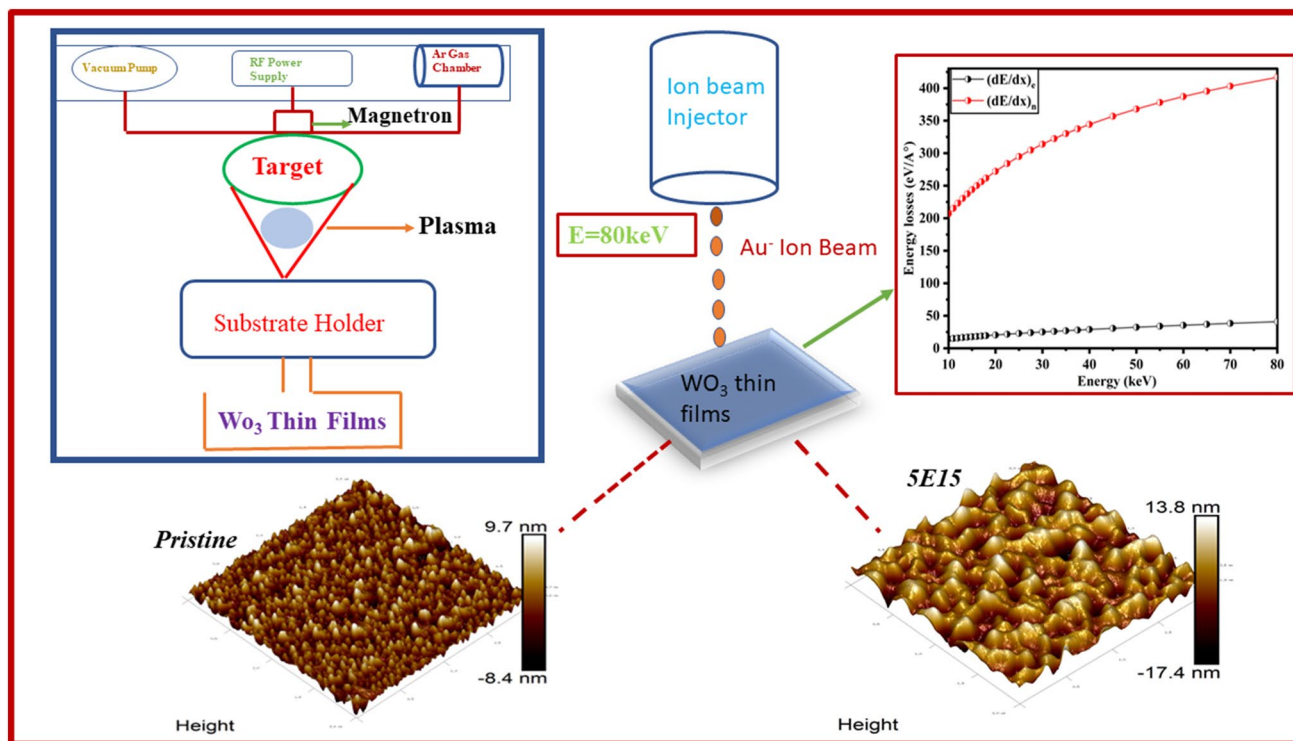


**Fig. 1** Schematics representing the experimental approach: (a) WO<sub>3</sub> thin films synthesized by RF-sputtering; (b) ion beam implantation of WO<sub>3</sub> thin films with various fluences, 5E14, 1E15, and 5E15 ions/cm<sup>2</sup> ; (c) energy loss generated by the effect of irradiation of thin films with low energy; (d) AFM spectra of pristine and ion beam implanted samples with varying fluences.

cm<sup>2</sup> ; (c) energy loss generated by the effect of irradiation of thin films with low energy; (d) AFM spectra of pristine and ion beam implanted samples with varying fluences.

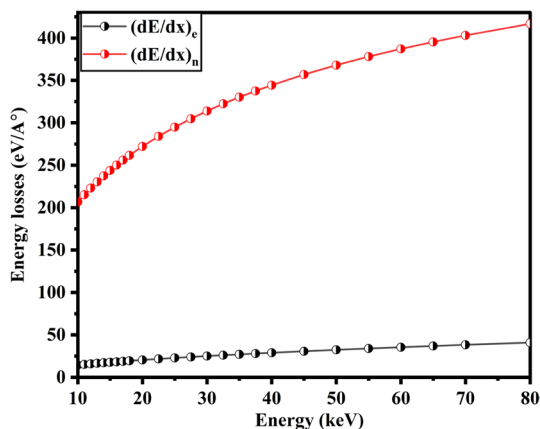


**Fig. 2** S<sub>c</sub> and S<sub>n</sub> plot of WO<sub>3</sub> thin film implanted by Au ion beam.

energy. Therefore, variation in the characteristics of thin films was caused by nuclear energy losses.

**Characterization Techniques**

The virgin and ion-implanted WO<sub>3</sub> thin films with energy of 80 keV by an Au ion beam at different fluences, 5E14, 1E15, and 5E15, were depicted by several methods such

as PL spectroscopy, AFM), UV-visible spectroscopy, XRD, XPS, and Raman spectroscopy. AFM was used to access the surface roughness and grain size of the thin film in tapping mode. The alteration in the optical characteristics of the WO<sub>3</sub> thin films was investigated by using a Hitachi U-3300 in the wavelength region (200–800 nm). Raman spectra of the thin film were carried out by a Renishaw In-Via Reflex micro-Raman spectrometer with a 488-nm Ar ion laser having a power of 50 mW and diffraction grating of 2400 lines/mm. The PL emission spectra of the WO<sub>3</sub> thin films were studied through the Perkin Elmer LS 55 fluorescence spectrometer having a wavelength range from 300 nm to 650 nm with an excitation wavelength of 420 nm. XPS was used to find the variation in electronic structure with an Omicron ESCA at MNIT Jaipur.

**Results and Discussion**

**X-ray Diffraction**

Using XRD, we investigated different factors such as crystal structure, full width half-maxima, dislocation density, and strain of the virgin WO<sub>3</sub> and implanted thin films. The XRD patterns of pristine WO<sub>3</sub> and the 80 keV implanted thin films

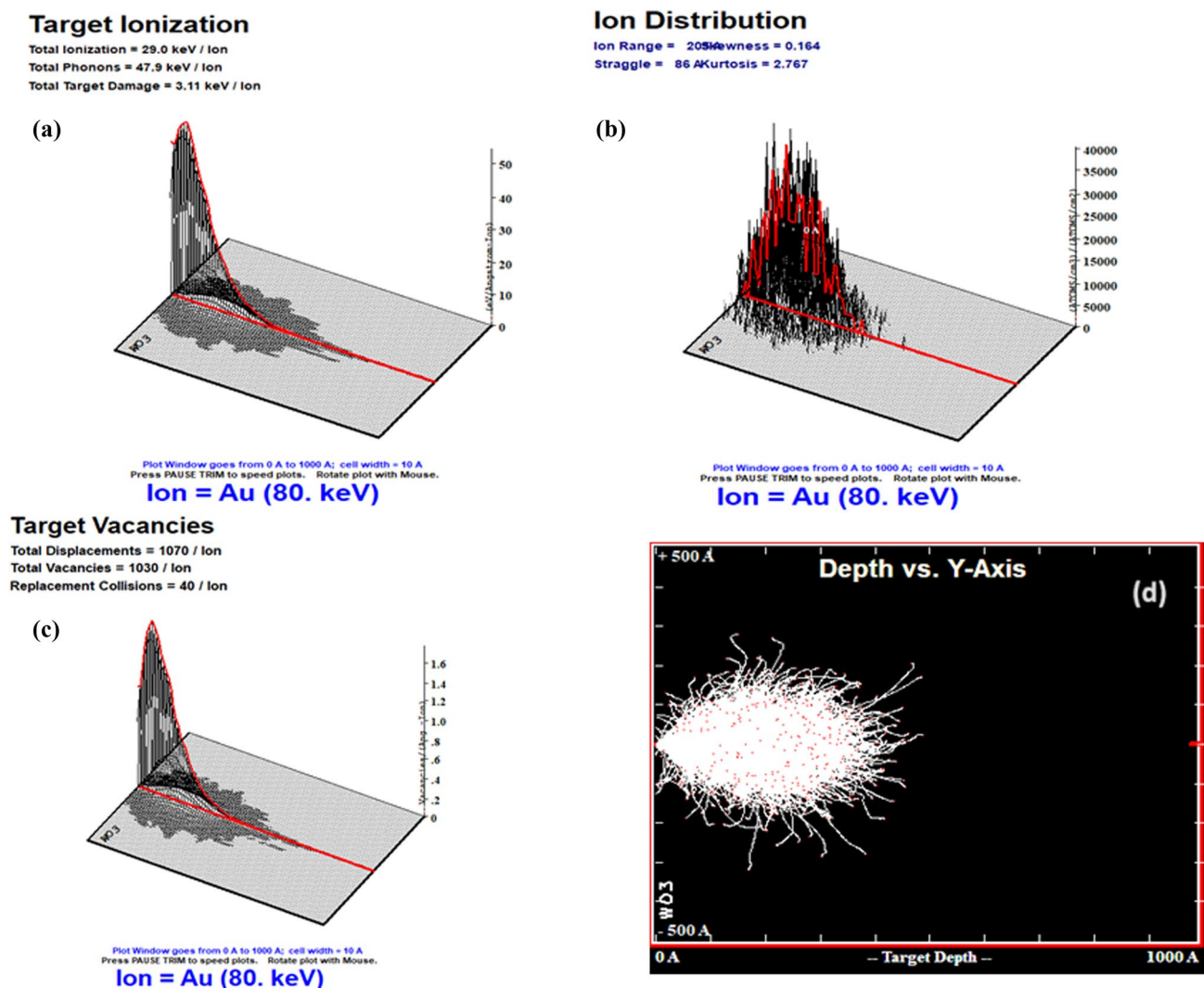


**Fig. 3** Plots of (a) target ionization (b) ion distribution (c) target vacancies and (d) path along the Y axis of WO<sub>3</sub> thin films.

at fluences, 5E14, 1E15, and 5E15, are displayed in Fig. 4. The XRD patterns of virgin and ion-implanted thin films at different fluences were recorded from 20° to 80°, showing their crystalline behavior. Un-implanted WO<sub>3</sub> thin films were found at peaks 24.36°, 28.9°, 34.06°, 41.7°, 45.8°, 50.1°, 55.7°, and 61.3° with the corresponding (200), (112), (202), (222), (320), (140), (420), and (143) planes. Our experimental data matched previously reported results with JCPDS No. 43–1035.<sup>52</sup> After ion beam implantation, no structural changes were observed up to the fluence of 5E15 ions/cm<sup>2</sup>. Miyakawa et al.<sup>52</sup> showed the reformation of the phases of thin films of WO<sub>3</sub> by helium ions or proton ions. We conclude from the literature that small changes in lattice parameters were observed by the Au ion beam because of distortion in the W-O frame. The intensity of the peaks at a fluences of 5E14, 1E15, and 5E15 sharply decreased, which shows the reduction in the crystalline nature of the samples after implantation and may also be owing to

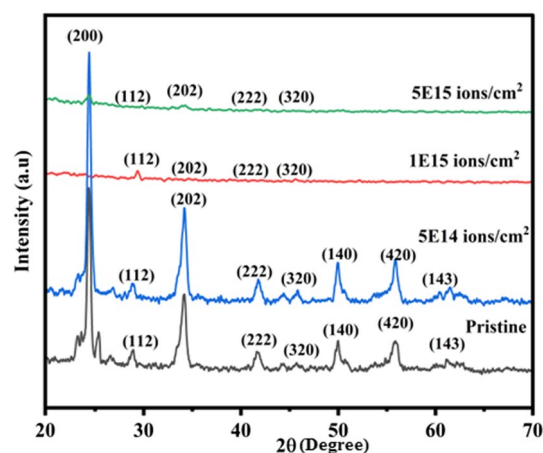


**Fig. 4.** XRD spectra of pristine WO<sub>3</sub> and the Au-implanted sample at various fluences of 5E14, 1E15, and 5E15.

damage created during ion beam implantation of the sample by 80 keV.<sup>53</sup> The devaluation in the intensity of peaks was observed due to the partial ordering of crystal and point defects and thermal vibration produced in the sample.

The crystallite size of the WO<sub>3</sub> and ion-implanted samples for the plane (200) were measured by using the Debye–Scherrer’s equation:

$$D = \frac{0.94\lambda}{\beta \cos \theta} \tag{1}$$

where  $\lambda$  is the wavelength of the X-ray,  $\beta$  is the full width half-maxima and  $\theta$  is the diffraction angle of the sample. The crystallite size of the WO<sub>3</sub> thin films before and after ion implantation are shown in Table I. The crystallite size of virgin WO<sub>3</sub> for the plane (200) was observed to be 20 nm. After the ion beam implantation of WO<sub>3</sub> thin films at different fluences, 5E14, 1E15, and 5E15, the crystallite size was decreased to 12.4 nm up to the fluence of 1E15 ions/cm<sup>2</sup>. The decrement in crystallite size after implantation by an Au ion beam with 80 keV energy is due to the effect of the Au ion beam which decreases the crystallinity of the sample. The crystallite size depleted after ion beam implantation is attributed to enhancement in the microstrain produced by implantation in the material which generates defects in the thin film.<sup>54</sup> Ion beam irradiation with an Au ion beam produces defects, mainly oxygen vacancies, in WO<sub>3</sub> thin films which can be due to the sputtering effect which reduces the crystallinity of the sample.<sup>31</sup> We have demonstrated that oxygen vacancies produced by ion beam irradiation can be used to improve the electrical conductivity. At a higher fluence of 5E15 ions/cm<sup>2</sup>, the peak vanishes, which shows the complete amorphization after ion beam implantation with 80 keV.<sup>55</sup> Identical observations were recorded by Solanki et al.<sup>56</sup>

The lattice strain and dislocation density of virgin and implanted WO<sub>3</sub> thin films at varying fluences of 5E14, 1E15, and 5E15 ions/cm<sup>2</sup> for the plane (200) are estimated by Eqs. 2 and 3:<sup>57</sup>

$$\epsilon = \beta/4 \tan\theta \tag{2}$$

$$\delta = 1/D^2 \tag{3}$$

where  $\epsilon$  is the strain,  $\theta$  is the diffraction angle,  $\delta$  represents the dislocation density, and  $D$  is the crystallite size of the sample. The lattice strain is generated by vacancies created due to the extra volume of grain boundaries, as reported by Singh et al.<sup>58</sup> The dislocation density decreases from pristine to 5E14 ions/cm<sup>2</sup> and fluctuations in the strain were noticed from pristine to irradiated samples at different fluences. The decrement in dislocation density with the fluence is due to the irradiation effect that generates more and more vacancies and enhancement in the demolition rate of the vacancies because of increases in density.

### UV Visible Spectroscopy

The optical study of WO<sub>3</sub> thin films in absorbance mode was carried out to study the variation in optical characteristics before and after exposure to irradiation at distinct fluences. The absorption spectra of virgin and irradiated WO<sub>3</sub> thin films at fluences 5E14, 1E15, and 5E15 are shown in Fig. 5a. The absorbance of WO<sub>3</sub> thin films decreases after exposure to ion beam irradiation at distinct fluences. At fluence 1E15 ions/cm<sup>2</sup>, the absorbance sharply decreases, which is attributed to an alteration in the optical band gap by Au ion beam implantation with 80 keV. The decrease in absorbance can be due to defects produced in the material by heat produced during the implantation of the thin films.<sup>59</sup>

The optical band gap of WO<sub>3</sub> thin films was investigated by the spectra of absorption and energy of photons by employing Tauc’s plot. The energy band gap of the sample was computed by using Tauc’s relationship:<sup>60,61</sup>

$$(\alpha h\nu)^n = B(h\nu - E_g) \tag{4}$$

where  $B$  is the proportionality constant,  $\alpha$  is the coefficient of absorption and determined by the relationship  $\alpha = 2.303 (A/t)$ , where  $A$  is the absorbance of the sample and  $t$  represents the thickness of the sample,  $\nu$  is the frequency,  $h$  is Plank’s constant,  $E_g$  is the optical band gap energy, and  $n$  shows the direct or indirect transition. For the direct band gap, the value of  $n$  is 2 and for  $n = 1/2$ , it has an indirect transition band. The alteration in the optical band gap of virgin and implanted WO<sub>3</sub> thin films at varying fluences 5E14, 1E15, and 5E15, is presented in Fig. 5b. The measured values of the direct band gap of virgin and WO<sub>3</sub>

**Table I** Full width half-maxima (FWHM), crystallite size, dislocation density and lattice strain for plane (200) for virgin and ion implantation with different fluences

Fluence (ions/cm <sup>2</sup> )	FWHM (radians)	Crystallite size (nm)	Dislocation density ( $\delta$ ) ( $\times 10^{16} \text{ m}^{-2}$ )	Strain ( $\times 10^{-2}$ )
Pristine	0.007	20.0	0.25	0.42
5E14	0.104	14.7	0.46	0.77
1E15	0.112	12.4	0.65	0.66
5E15	–	–	–	–

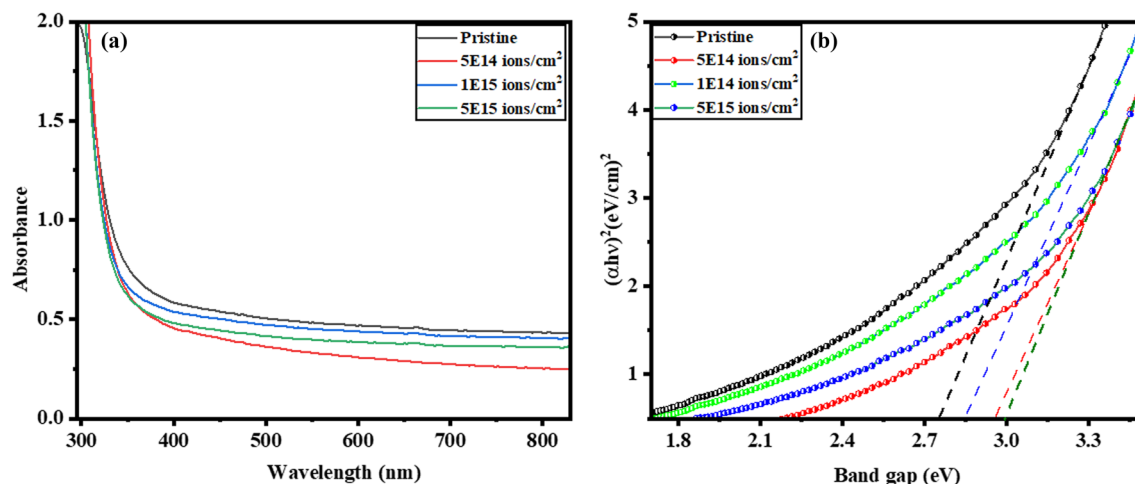


**Fig. 5** (a) Absorbance versus wavelength of pristine and ion beam-implanted thin films. (b) Band gap alteration of un-implanted and Au ion beam-implanted WO<sub>3</sub> thin films.

ion-implanted thin films with 80 keV are shown in table II. The band gap values of WO<sub>3</sub> virgin and implanted thin films lie in the region from 2.75–2.99 eV. The optical energy band gap value of WO<sub>3</sub> thin films increases from pristine to 5E15 ions/cm<sup>2</sup> except for implantation at fluence 1E15 ions/cm<sup>2</sup>. The enhancement in the band gap was explained by the mechanism that arises during the implantation of the thin films. The energy was transferred by incident ions which produce latent tracks with high temperature compared with the environment. As a result of this, the defects in the forbidden space produce localized states near the conduction and valence bands. During ion beam exposure of the thin films, the heat treatment of defects occurs, which disassociates the conduction band and valence band's energy level and causes an increase in the optical energy band gap.<sup>62,63</sup> The reduction in band gap at 1E15 ions/cm<sup>2</sup> was observed and can be explained by the Davis–Mott model.<sup>64</sup> When the interaction of ions takes place with the sample, it produces local disorder in the system. The Davis–Mott model shows that the increase in ion fluence produces enhancement in local disorder, which increases the localized energy states in the forbidden space, causing the band-gap depletion of the sample.<sup>65</sup>

Urbach energy ( $E_u$ ) provides significant band gap details and its composition from the absorption spectra of the thin films. In the optical band gap region, an exponential curve with the absorption coefficient curve was observed, called the Urbach tail. The Urbach tail has been detected because of various factors like disordered, impoverished crystalline, and amorphous nature of the material.<sup>66,67</sup> In the ion beam implantation process, localized energy states arise in the energy band gap causing the broadening of absorption spectra and producing a sub-energy band gap absorption

**Table II** The direct band gap and Urbach energy measured value of un-implanted and Au ion beam-implanted thin films at various fluences.

Fluence	Direct band gap (eV)	Urbach energy (eV)
Pristine	2.75	2.33
5E14	2.95	1.12
1E15	2.85	1.40
5E15	2.99	1.58

tail known as Urbach energy.<sup>68</sup> Urbach energy can be estimated by Eqs. 5 and 6<sup>69</sup> and shown in Fig. 6a:

$$\alpha = \alpha_0 \exp(h\nu/E_u) \quad (5)$$

$$\ln \alpha = \ln \alpha_0 \exp(h\nu/E_u) \quad (6)$$

where  $E_u$  is the Urbach energy,  $\alpha_0$  is a constant, and  $\alpha$  the absorption coefficient. The plot of  $\ln \alpha$  versus photon energy is shown in Fig. 6a. The estimated values of Urbach energy of virgin and implanted WO<sub>3</sub> thin films at varying fluences, 5E14 ions/cm<sup>2</sup>, 1E15 ions/cm<sup>2</sup>, and 5E15 ions/cm<sup>2</sup>, are displayed in Table II. The variation in Urbach energy after implantation at different ion fluences was observed because of variation in the defects states in the forbidden energy state.<sup>70</sup>

The thickness at which the optical density value is equal to 1/e at the surface of the sample is known as the penetration depth or skin depth. The skin depth of the thin films leans on conductivity which is based on the energy band gap. The skin depth specifies that, when the electromagnetic waves cover the thickness of the thin films, their amplitude reduces.<sup>71</sup> The penetration depth is computed by the

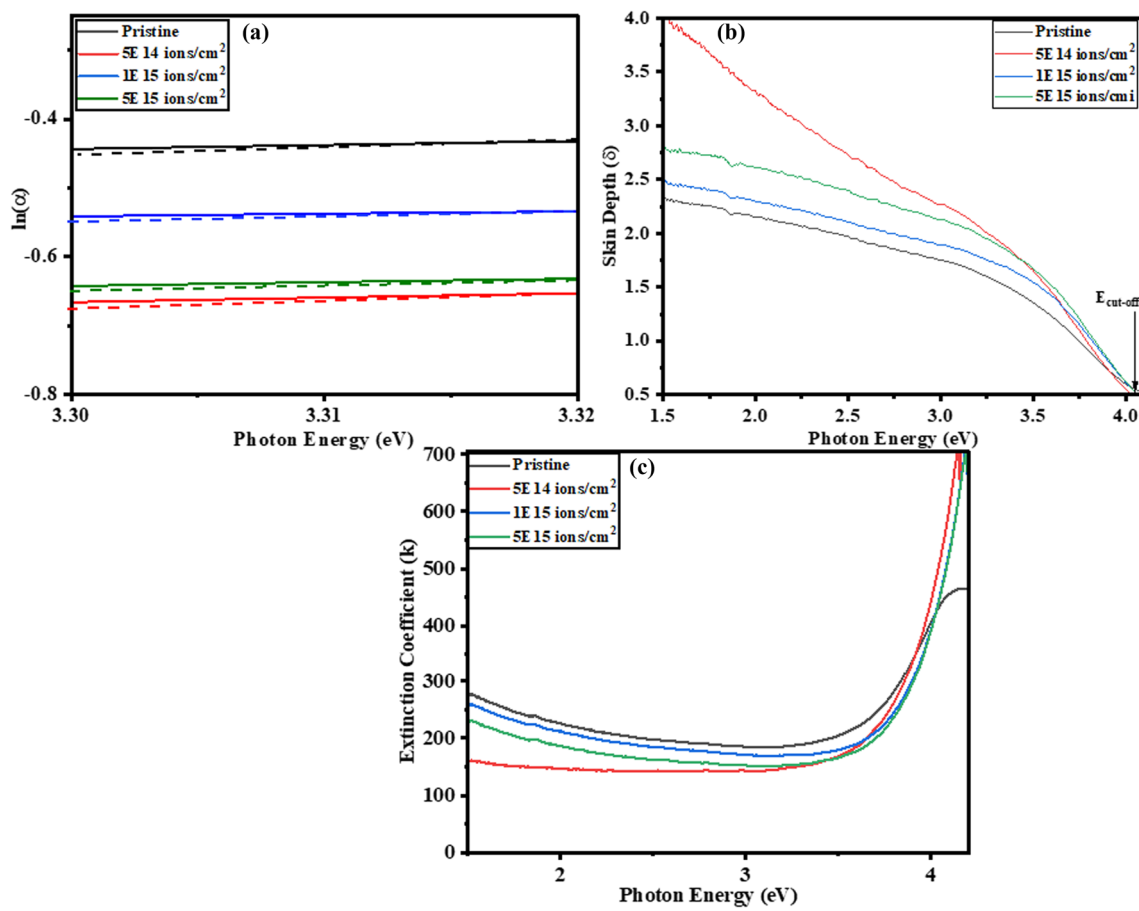


**Fig. 6** (a) The plot of Urbach's energy of un-implanted and Au ion beam implanted thin films at different fluences. (b) The modifications in skin depth with photon energy of pristine and implanted WO<sub>3</sub> thin

films. (c) Alteration in extinction coefficient with photon energy of virgin and Au ion beam-implanted WO<sub>3</sub> thin films.

relationship plot of skin depth versus photon energy of virgin and implanted WO<sub>3</sub> thin films with 80 keV, as displayed in Fig. 6b, from which we can see that the increment in skin depth with photon energy was observed until it reached the maximum level and then decreased to zero with increasing photon energy. The value of energy at which skin depth is zero is known as cut-off energy.<sup>67</sup> The calculated value of cut-off energy was observed to be 4.06 eV for the pristine WO<sub>3</sub> thin film. After ion beam implantation, the variation in height and position of the thin film was observed. The maximum height after implantation was observed at fluence 5E14 ions/cm<sup>2</sup>.

The extinction coefficient ( $k$ ) is used for determining some optical measurements. It determines the fraction of the loss of light because of the absorption and scattering process of light. The plot of extinction coefficient versus photon energy of virgin and implanted WO<sub>3</sub> thin films at different fluences, 5E14, 1E15, and 5E15, is displayed in Fig. 6c. The extinction coefficient was calculated by the equation  $k = \alpha\lambda/4\pi$ .<sup>72</sup> The value of the extinction coefficient

decreased with the enhancement in photon energy and ion fluence. The value of extinction coefficient was a maximum for pristine WO<sub>3</sub> thin film and a minimum at fluence 5E14 ions/cm<sup>2</sup>. It was found that variation in the extinction coefficient arises due to the effect of ion beam implantation.<sup>70</sup>

### PL Spectroscopy

To investigate the nature of defects present in the specimen, PL analysis was carried out at ambient temperature. PL spectroscopy is used for getting information about the recombination of electron-hole pairs by inducing photon energy. The electron-hole pair recombination rate is directly related to the PL intensity of the thin film samples.<sup>73–75</sup> Photoluminescence spectroscopy is also used to determine various defects present in the sample, such as impurities, vacancies, interstitials, and the crystal quality of the thin films and the electronic energy band gap. The PL spectra of the virgin WO<sub>3</sub> and ion-implanted thin films at varying fluences, 5E14, 1E15, and 5E15, were taken in the wavelength

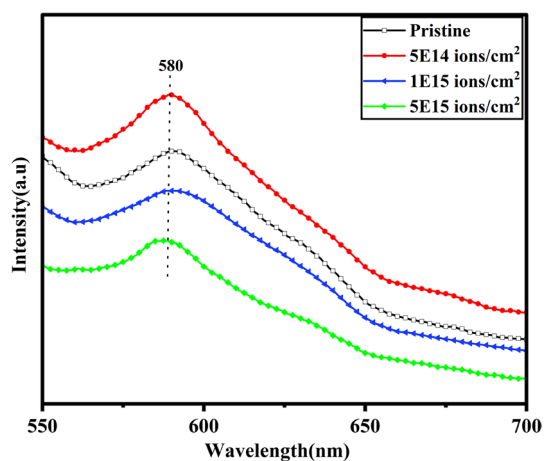


**Fig. 7** PL spectra of pristine and implanted  $\text{WO}_3$  thin films with 80 keV  $\text{Au}^+$  ions with varying fluence.

range from 380 nm to 700 nm at an excitation wavelength of 420 nm, as illustrated in Fig. 7. The emission band was observed at 580 nm for pristine and low-energy irradiated  $\text{WO}_3$  thin films with fluence from pristine to  $5\text{E}15$  ions/ $\text{cm}^2$ . The observed emission band was associated with the localized states arising from the singly charged oxygen vacancies in the sample.<sup>76</sup> Oxygen vacancies have the ability to capture the excitation energy, and light can be released directly by recombination with the valence band. After implantation

by the Au ion beam, the PL intensity of the  $\text{WO}_3$  thin film increases at fluence  $5\text{E}14$ , and this increase in PL intensity was detected by virtue of the enhancement in the defects concentration, whole oxygen vacancies appear in the sample arising from the Au ion beam implantation. The reduction in PL intensity for the fluences  $1\text{E}15$  and  $5\text{E}15$  was observed because of defects formation which behave like a non-radiative recombination center and, because of increases in the ion fluence of the sample, the centers' concentration increases.<sup>77</sup> The variation in PL intensity was seen because of enhancement in oxygen vacancies after Au ion beam irradiation of the sample. The PL intensity decrement can be attributed to the demolishing of the defects by heating generated during ion implantation of the thin films.<sup>78</sup>

### Atomic Force Microscopy

AFM spectroscopy was employed for the morphological study of the virgin and 80 keV Au ion-implanted  $\text{WO}_3$  thin films at different fluences,  $5\text{E}14$ ,  $1\text{E}15$ , and  $5\text{E}15$ . The force and potential energy between the sample surface and the small tip were evaluated by a probe identified as a cantilever. The cantilever tip employs repulsive or attractive forces by moving on the shallow part of the thin films. The 3D image of virgin and implanted  $\text{WO}_3$  thin films at varying fluence is shown in Fig. 8.

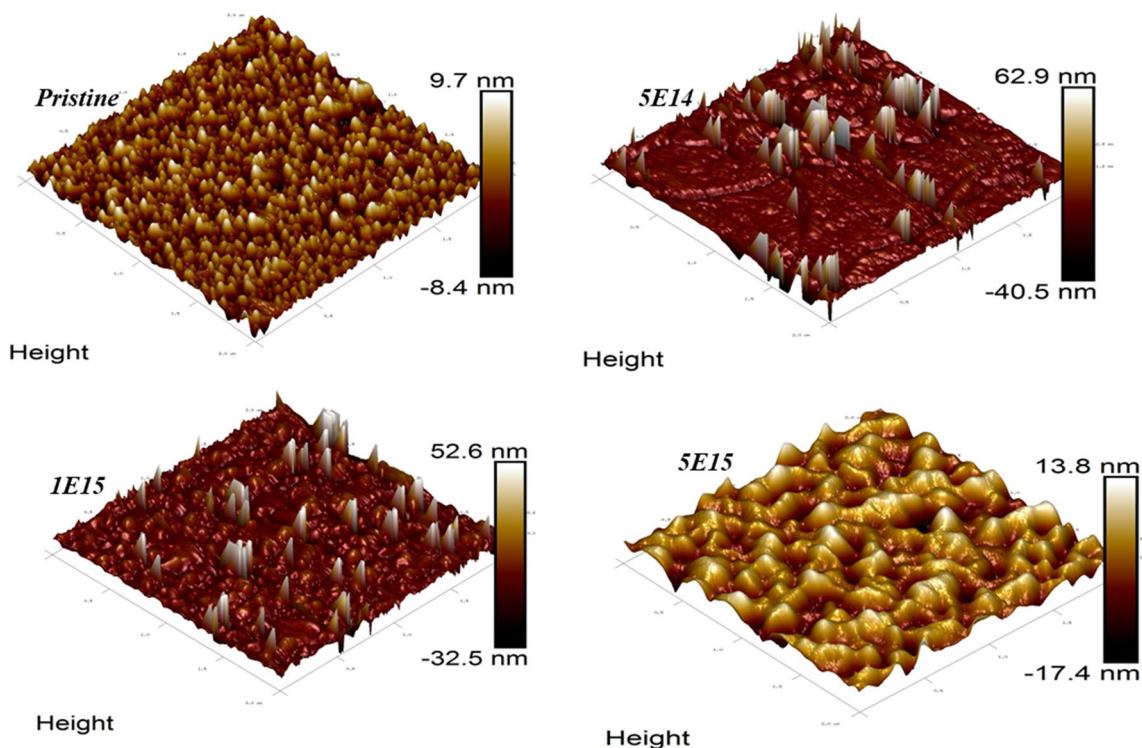


**Fig. 8** The AFM images of 3-dimensional virgin and Au ion beam-irradiated  $\text{WO}_3$  thin films at different fluence from pristine to  $5\text{E}15$  ions/ $\text{cm}^2$ .



Modification in the average surface roughness and root mean square value was observed with distinct fluence. For the pristine  $\text{WO}_3$  thin film, the average roughness ( $R_a$ ) was 16.3 nm, and at higher fluence of  $5\text{E}15$  ions/ $\text{cm}^2$  it became 14.5 nm. The devaluation in the surface roughness was recognized because of the surface diffusion due to material transportation.<sup>79,80</sup> The roughness depletion may be due to a discontinuous track which produces defects like color centers.<sup>81</sup>

The plot of log-normal fitting of virgin and implanted thin films is displayed in the bar graph in Fig. 9. The grain size of the pristine  $\text{WO}_3$  was measured at 49.5 nm and, after implantation with Au ion beam at the higher fluence  $5\text{E}15$  ions/ $\text{cm}^2$ , it was 56.6 nm. In ion beam exposure with low energy, point defects were produced by losses created by nuclear energy which enhanced the size of the grains. The variation in the grain size after implantation occurs because, as the energy was transferred by the incident ion, cluster malfunction takes place.<sup>82</sup> The enhancement in grain size was because the secondary electron transfers their kinetic energy to the lattice atom from the target by the e'-phonon interaction process with the irradiation and this causes an increment in the lattice temperature of the materials resulting in morphological variation in the sample after exposure to ion irradiation. The increase in the grain size after implantation can be ascribed to the addition in the density of defects known as vacancies that act as nucleation centers for the nanocrystallization of the thin films. Liu et al. observed an increment in the grain size when Cu thin films were treated by an  $\text{Ar}^+$  ion beam with an energy of 200 keV.<sup>83</sup> The increment in grain size can be due to the quenching effect produced after the bombardment of high-energy ions.

## Raman Spectroscopy

Raman spectroscopy was used for structural analysis such as phase formation and Raman shift in the band of the thin films. Raman spectroscopy of virgin and implanted  $\text{WO}_3$  thin film with fluences  $5\text{E}14$ ,  $1\text{E}15$ , and  $5\text{E}15$  is displayed in Fig. 10. Raman spectra of unirradiated  $\text{WO}_3$  thin film show two bands, one in the lower wavelength region ( $100\text{--}500\text{ cm}^{-1}$ ) and one in the higher wavelength region ( $500\text{--}900\text{ cm}^{-1}$ ). The vibrational peak found lower than  $200\text{ cm}^{-1}$  corresponds to lattice modes and the peak above the frequency range  $200\text{ cm}^{-1}$  is related to stretching mode and deformation in the sample. For virgin  $\text{WO}_3$  thin films, the bands detected at  $268\text{ cm}^{-1}$  and  $325\text{ cm}^{-1}$  correspond to the O-W-O bending mode of  $\delta(\text{W}^{6+}\text{-O})$ . The peaks obtained at wavenumbers  $714\text{ cm}^{-1}$  and  $807\text{ cm}^{-1}$  were due to  $\delta(\text{W}^{6+}\text{-O})$  stretching modes. The peak at  $520.5\text{ cm}^{-1}$  is related to the optical phonon zone of the silicon substrate. A sharp intensity peak was observed at  $807\text{ cm}^{-1}$  which shows the monoclinic nature of the  $\text{WO}_3$  thin films.<sup>61</sup> Our results are matched with former reported  $\text{WO}_3$  results.<sup>84</sup> After implantation of  $\text{WO}_3$  thin films with Au ions, a small shifting of peaks was observed at fluences  $5\text{E}14$  and  $1\text{E}15$  which signifies the red shift in the thin films. The red shift was observed because of the oxygen vacancies produced when exposed to ion beam irradiation.<sup>61</sup> The alteration in the Raman intensity was observed at fluences  $5\text{E}14$  and  $1\text{E}15$  because of ion implantation defects produced on the surface of the thin films.<sup>85</sup> At higher fluence  $5\text{E}15$ , the Raman peaks completely vanish because of the amorphization of the  $\text{WO}_3$  thin films which is ascribed to the large density of defect formation during the implantation of the thin films.<sup>86</sup> The

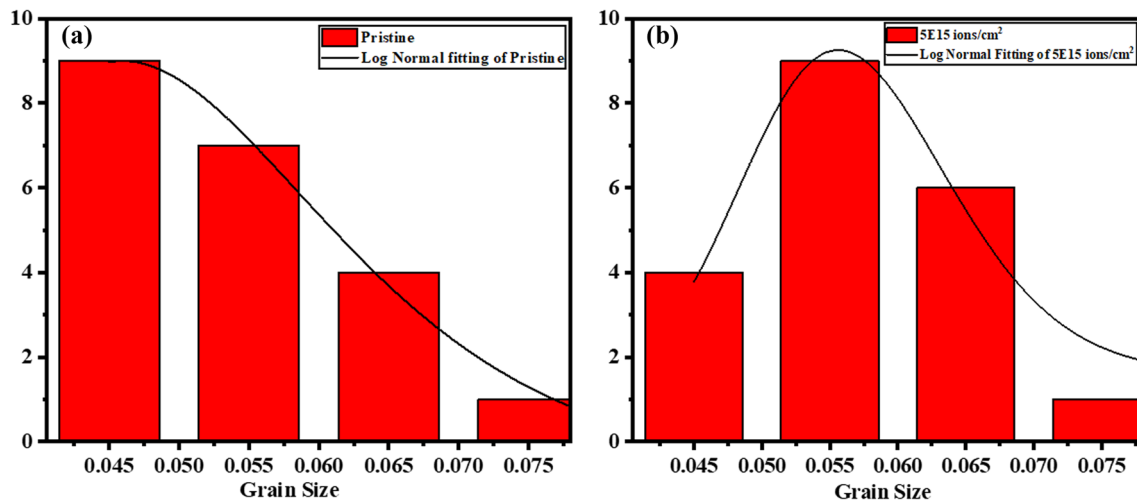
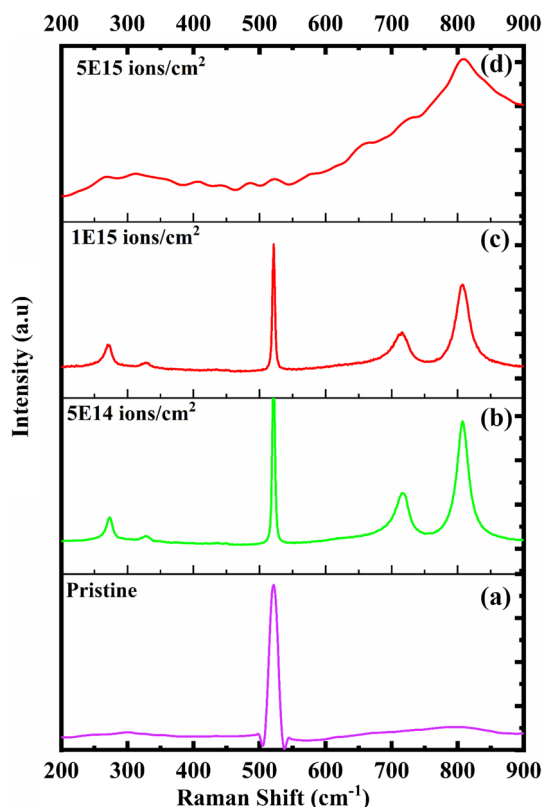
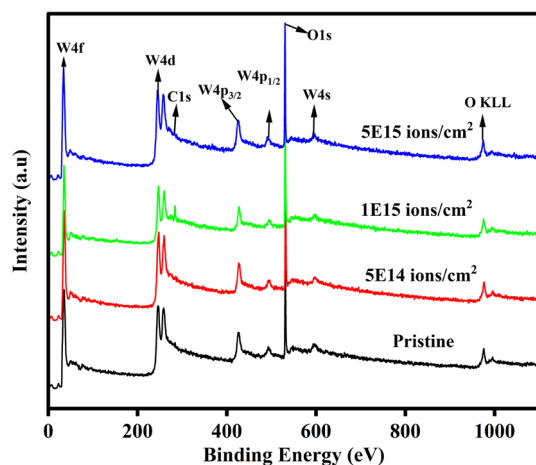


Fig. 9 Log-normal fitting of un-implanted and ion beam-irradiated thin films: (a) virgin  $\text{WO}_3$  thin films, (b)  $5\text{E}15$  ions/ $\text{cm}^2$ .



**Fig. 10** Raman spectra of a virgin and implanted sample at different fluence: (a) pristine; (b) 5E14 ions/cm<sup>2</sup>; (c) 1E15 ions/cm<sup>2</sup>; and (d) 5E15 ions/cm<sup>2</sup>.



**Fig. 11** Survey spectra of un-implanted and implanted thin films at fluences 5E14, 1E15, and 5E15.

broadening of Raman peaks with intensity shows the reduction in crystallite size matched with the XRD results.

## XPS Spectroscopy

The valence state of the W atoms and oxygen vacancies in the pristine and implanted thin films was identified by XPS spectroscopy, which provides elemental composition information in the WO<sub>3</sub> virgin and ion-implanted thin films at fluences 5E14, 1E15, and 5E15. The XPS measurements of the thin films were carried out with 20-mA current, 15-kV voltage, and a chamber temperature fixed at 24 °C. The virgin and implanted samples at different fluences were degassed in vacuum (5.2 E–10 mbar) overnight.

The XPS survey spectra of the unirradiated and irradiated thin films with 80 keV at varying fluences are displayed in Fig. 11. The survey spectra of the RF-sputtered WO<sub>3</sub> thin films depict the existence of W, O, and C atoms. The observed peaks were W4f, W4d, C1s, W4p<sub>3/2</sub>, W4p<sub>1/2</sub>, O1s, W4s, and O KLL with the binding energies of 33.3 eV, 244 eV, 284 eV, 426.6 eV, 495.3 eV, 531.6 eV, 597 eV, and 976.1 eV, respectively. At the binding energy 976.1 eV, the O KLL peak shows a series of Auger peaks. The obtained results are consistent with previously reported results.<sup>87</sup> The XPS survey spectra show no transformation in the spectra before and after implantation of WO<sub>3</sub> thin films at lower or higher fluences.

The high-resolution spectra of tungsten and oxygen are displayed in Fig. 12a and b. The XPS spectra demonstrate two prominent peaks, W4f<sub>7/2</sub> and W4f<sub>5/2</sub>, for the virgin and implanted WO<sub>3</sub> thin films at distinct fluence. The oxygen peak (O1s) was obtained at 531 eV for pristine WO<sub>3</sub> thin films, while for higher fluence 5E15 ions/cm<sup>2</sup>, it was observed to be 530 eV. The core level with their binding energy for implanted WO<sub>3</sub> thin films at fluences 5E14, 1E15, and 5E15 is displayed in Table III. The shifting in the tungsten peak was observed after implantation with 80 keV at varying fluences, which may be due to variation in the electronic structure of the nanocrystals which also alters the binding energy. From the figure, we can notice that the tungsten atom contains more than one peak, which shows the existence of a more valence state of the W atom. After deconvolution of the pristine WO<sub>3</sub> and higher fluence 5E15 thin films, as illustrated in Fig. 13a and b, the W 4f spectra show two tungsten species, W<sup>6+</sup> and W<sup>5+</sup>, with binding energies 35.9 eV, 34 eV, 32.4 eV, and 31.7 eV.<sup>88</sup> The presence of W<sup>5+</sup> atoms was observed because the deficiency of oxygen occurs during the deposition of the thin films.<sup>89</sup>

## Conclusions

RF-sputtered WO<sub>3</sub> thin films were irradiated with fluences of 5E14, 1E15, and 5E15 by 80 keV energy to study the consequences of a low Au ion beam on the structural, optical, and morphological traits of pristine and irradiated WO<sub>3</sub> thin

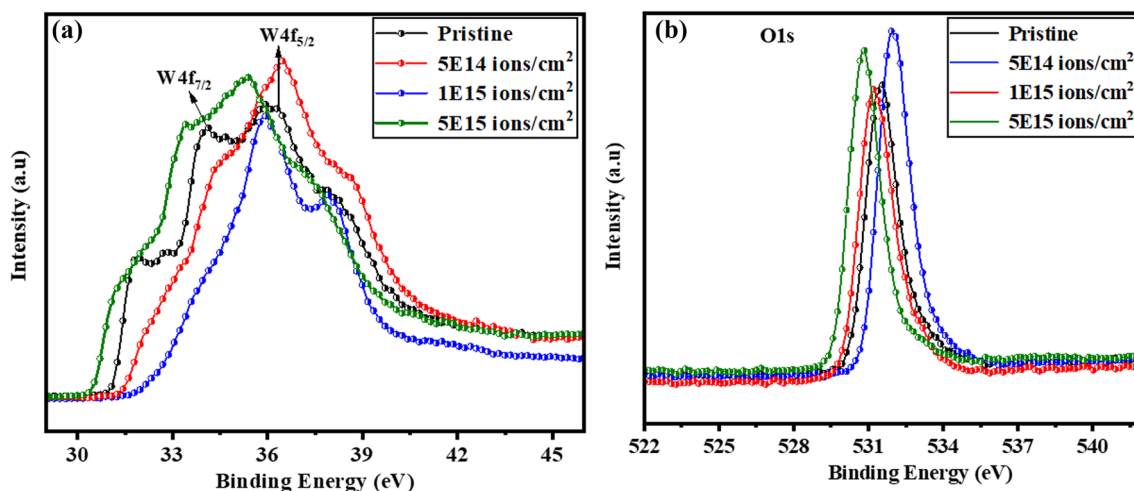


**Fig. 12** High-resolution spectra of (a) W atoms with varying fluence and (b) O atoms of the pristine and implanted WO<sub>3</sub> thin film at fluences 5E14, 1E15, and 5E15.

**Table III.** The orbital splitting and binding energy of implanted and un-implanted thin films with 80 keV.

Sample	Binding energy (W4f <sub>7/2</sub> )	Binding energy (W4f <sub>5/2</sub> )	Spin-orbit splitting (δ4f)
Pristine	34.1 eV	36.1 eV	2.0
5E14 ions/cm <sup>2</sup>	34.5 eV	36.4 eV	1.9
1E15 ions/cm <sup>2</sup>	35.9 eV	37.9 eV	2.0
5E15 ions/cm <sup>2</sup>	33.4 eV	36.3 eV	2.9

films. When the thin films were subjected to ion beams with low energy, the nuclear loss was greater than the electronic energy losses. AFM spectra showed that the roughness

of the WO<sub>3</sub> thin films after implantation decreased from 16.3 nm to 14.5 nm. The size of the grains was enhanced after implantation from pristine to 5E15 ions/cm<sup>2</sup> from 49.5 nm to 56.6 nm. The XRD showed the reduction in crystallite size from pristine to fluence of 1E15 ions/cm<sup>2</sup> from 20 nm to 12.4 nm, and at 5E15 ions/cm<sup>2</sup>, the peak completely vanishes because of implantation at 80 keV. In PL spectroscopy, an emission band was observed at 580 nm and, after implantation with an Au ion beam, an enhancement in the intensity was observed at fluence 5E14 ions/cm<sup>2</sup>. From the optical study, several characteristics of the WO<sub>3</sub> thin film were observed, such as absorbance, Urbach energy, skin depth, and extinction coefficient. The absorbance of the WO<sub>3</sub> thin film after implantation by the Au ion beam decreased due to variations in the optical band gap and the generation of defects during ion beam implantation. The

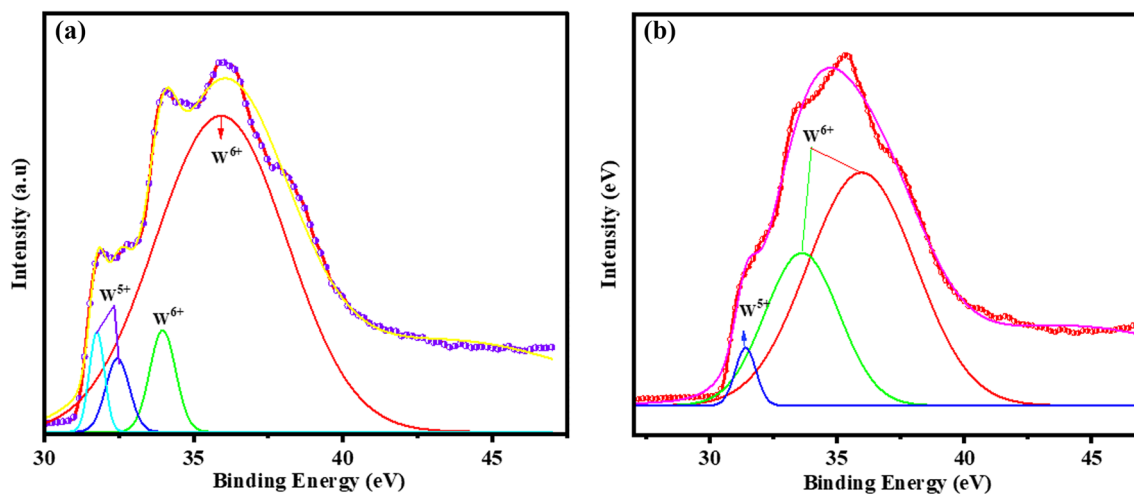


**Fig. 13** (a) Deconvoluted spectra of pristine WO<sub>3</sub> thin film. (b) Deconvoluted spectra of WO<sub>3</sub> thin film at fluence 5E15 ions/cm<sup>2</sup>.

band gap alteration from virgin to implanted WO<sub>3</sub> thin film was observed in the range from 2.75 eV to 2.99 eV. Raman spectra of the virgin and ion irradiated sample showed the monoclinic structure with a prominent peak at 807 cm<sup>-1</sup>. Variation in Raman intensity at fluences 5E14 and 1E15 was observed and it completely vanishes at fluence 5E15 ions/cm<sup>2</sup> because the WO<sub>3</sub> thin film was completely amorphized. XPS study showed the shifting in the tungsten peak after implantation with 80 keV at varying fluences, which may be due to variation in the electronic structure of the nanocrystals which also alters the binding energy.

### Future Prospectives

The ion beam treatment is an effective progressive method that has a variety of applications in the semiconductor industry. Various defects and dopants in semiconductors have been created by the ion beam irradiation process for the fabrication of nanostructures or microstructures. However, recent research shows that it is a powerful tool for thin films and is also used for a variety of applications, such as superconductivity, piezoelectricity, metal–insulator transition, and gas-sensing properties.<sup>90</sup> The characteristics of metal oxide semiconductors are tuned by ion beam treatment by modifying their electron density, lattice distortion, and defect states. Various research groups have applied the ion beam technique to increase the performance of metal oxide thin films. Metal oxide semiconductors such as ZnO,<sup>91</sup> SnO<sub>2</sub>,<sup>92</sup> TiO<sub>2</sub>,<sup>93</sup> and In<sub>2</sub>O<sub>3</sub><sup>94</sup> have been greatly used in the field of gas sensors, such as nitrogen dioxide sensors,<sup>95</sup> oxygen sensors,<sup>96</sup> LPG sensors,<sup>97</sup> carbon monoxide sensors,<sup>77</sup> etc. In future, we will study the gas-sensing properties of WO<sub>3</sub> thin films irradiated at different fluences for various gases such as CO<sub>2</sub>, NH<sub>3</sub>, and NO<sub>2</sub>. Sensor properties like selectivity, stability, reversibility, and sensitivity depend upon crystallinity, vacancies, porosity, surface morphology, electronic characteristics, and thin-film thickness characteristics. The ion beam treatment method enhances the performance of the sensor by reducing thin-film resistivity, decreasing grain size, improving gas sensitivity, and so on.<sup>98</sup>

**Acknowledgments** One of the authors Prof. Rajesh Kumar is thankful to the Department of Science and Technology (DST-SERB-CRG), Govt. of India, File Number: CRG/2022/002906), New Delhi, Inter University Accelerator Center, New Delhi, File No. IUAC/XII.3A/68308 and Guru Gobind Singh Indraprastha University, New Delhi, for providing the FRGS Grant. One of the authors Deepika is thankful to the University Grants Commission (UGC) Govt. of India, New Delhi for providing financial support (UGC-SRF Fellowship). The authors are also thankful to the Inter-University Accelerator Center for the optical measurements and Ion beam facility.

**Author contributions** DD: Experimental & Investigation, Formal analysis RK: Experimental plan, Manuscript draft correction, visualization, and supervision.

**Conflict of interest** The author declare that they have no conflict of interest.

**Ethical Approval** Not Applicable

### References

1. D.S. Martínez, A. Martínez-De La Cruz, and E.L. Cuéllar, Photocatalytic properties of WO<sub>3</sub> nanoparticles obtained by precipitation in presence of urea as complexing agent. *Appl. Catal. A: General* 398(1–2), 179–186 (2011).
2. D. Sánchez-Martínez, A. Martínez-De La Cruz, and E. López-Cuéllar, Synthesis of WO<sub>3</sub> nanoparticles by citric acid-assisted precipitation and evaluation of their photocatalytic properties. *Mater. Res. Bull.* 48(2), 691–697 (2013).
3. A.B.D. Nandiyanto, F. Triawan, R. Firly, A.G. Abdullah, Y. Aono, K. Inaba, and K. Kishimoto, Identification of micro-mechanical characteristics of monoclinic tungsten trioxide microparticles by nanoindentation technique. *Mater. Phys. Mech.* 42(3), 323–329 (2019).
4. H.O. Tekin, M.I. Sayyed, and S.A.M. Issa, Gamma radiation shielding properties of the hematite-serpentine concrete blended with WO<sub>3</sub> and Bi<sub>2</sub>O<sub>3</sub> micro and nano particles using MCNPX code. *Rad. Phys. Chem.* 150, 95–100 (2018).
5. N.A. Shik and L. Gholamzadeh, X-ray shielding performance of the EPVC composites with micro-or nanoparticles of WO<sub>3</sub>, PbO or Bi<sub>2</sub>O<sub>3</sub>. *Appl. Radiat. Isot.* 139, 61–65 (2018).
6. D. Sánchez-Martínez, A. Martínez-De La Cruz, and E. López-Cuéllar, Synthesis of WO<sub>3</sub> nanoparticles by citric acid-assisted precipitation and evaluation of their photocatalytic properties. *Mater. Res. Bull.* 48(2), 691–697 (2013).
7. D.B. Hernandez-Uresti, D. Sánchez-Martínez, A. Martínez-De La Cruz, S. Sepúlveda-Guzmán, and L.M. Torres-Martínez, Characterization and photocatalytic properties of hexagonal and monoclinic WO<sub>3</sub> prepared via microwave-assisted hydrothermal synthesis. *Ceram. Int.* 40(3), 4767–4775 (2014).
8. M.C. Rao, Structure and properties of WO<sub>3</sub> thin films for electrochromic device application. *J. Non-Oxide Glasses* 5, 1–8 (2013).
9. H.H. Lu, Effects of oxygen contents on the electrochromic properties of tungsten oxide films prepared by reactive magnetron sputtering. *J. Alloy. Compd.* 465(1–2), 429–435 (2008).
10. P.M. Woodward, A.W. Sleight, and T. Vogt, Ferroelectric tungsten trioxide. *J. Solid State Chem.* 131(1), 9–17 (1997).
11. K. Yuan, C.Y. Wang, L.Y. Zhu, Q. Cao, J.H. Yang, X.X. Li, and D.W. Zhang, Fabrication of a micro-electromechanical system-based acetone gas sensor using CeO<sub>2</sub> nanodot-decorated WO<sub>3</sub> nanowires. *ACS Appl. Mater. Interfaces.* 12(12), 14095–14104 (2020).
12. Y. Zhao, G. Brocks, H. Genuit, R. Lavrijsen, M.A. Verheijen, and A. Bieberle-Hütter, Boosting the performance of WO<sub>3</sub>/n-Si heterostructures for photoelectrochemical water splitting: from the role of Si to interface engineering. *Adv. Energy Mater.* 9(26), 1900940 (2019).
13. C. Ge, M. Wang, S. Hussain, Z. Xu, G. Liu, and G. Qiao, Electron transport and electrochromic properties of sol-gel WO<sub>3</sub> thin films: effect of crystallinity. *Thin Solid Films* 653, 119–125 (2018).
14. B.W.C. Au, A. Tamang, D. Knipp, and K.Y. Chan, Post-annealing effect on the electrochromic properties of WO<sub>3</sub> films. *Opt. Mater.* 108, 110426 (2020).
15. B. Qu, H. Du, T. Wan, X. Lin, A. Younis, and D. Chu, Synaptic plasticity and learning behavior in transparent tungsten oxide-based memristors. *Mater. Des.* 129, 173–179 (2017).

16. M. Karimi-Nazarabad and E.K. Goharshadi, Highly efficient photocatalytic and photoelectrocatalytic activity of solar light driven WO<sub>3</sub>/g-C<sub>3</sub>N<sub>4</sub> nanocomposite. *Sol. Energy Mater. Sol. Cells* 160, 484–493 (2017).
17. S. Wang, T. Wang, Y. Liu, Y. Gao, Y. Ding, X. Xu, and W. Chen, Visible light-driven photodecomposition system: preparation and application of highly dispersed Pt-loaded WO<sub>3</sub> microparticles. *Micro & Nano Letters* 6(4), 229–232 (2011).
18. M.B. Tahir, M. Sagir, and N. Abas, Enhanced photocatalytic performance of CdO-WO<sub>3</sub> composite for hydrogen production. *Int. J. Hydrogen Energy* 44(45), 24690–24697 (2019).
19. M.B. Tahir et al., WO<sub>3</sub> nanostructures-based photocatalyst approach towards degradation of RhB dye. *J. Inorg. Mater.* 28(3), 1107–1113 (2018).
20. V. Iliev, D. Tomova, S. Rakovsky, A. Eliyas, and G.L. Puma, Enhancement of photocatalytic oxidation of oxalic acid by gold modified WO<sub>3</sub>/TiO<sub>2</sub> photocatalysts under UV and visible light irradiation. *J. Mol. Catal. A: Chem.* 327(1–2), 51–57 (2010).
21. Y. Wu, Y. Wei, Q. Guo, H. Xu, L. Gu, F. Huang, and J. Wu, Solvothermal fabrication of La-WO<sub>3</sub>/SrTiO<sub>3</sub> heterojunction with high photocatalytic performance under visible light irradiation. *Sol. Energy Mater. Sol. Cells* 176, 230–238 (2018).
22. M. Takacs and A.E. Pap, Gas sensitivity of sol-gel prepared mesoporous WO<sub>3</sub> thin film. *Procedia Eng.* 168, 289–292 (2016).
23. H. Zhang, Y. Li, G. Duan, G. Liu, and W. Cai, Tungsten oxide nanostructures based on laser ablation in water and a hydrothermal route. *CrystEngComm* 16(12), 2491–2498 (2014).
24. L.C. Klein, *Mater. Manuf. Process.* 9, 1007 (1994).
25. P. Limnonthakul, W. Luangtip, C. Puttharugsa, I. Lutchanont, C. Chananonawathorn, P. Eiamchai, S. Limwichean, V. Pattantseakul, and M. Horprathum, Influence of oxygen flow rate on electrochromic property of WO<sub>3</sub> nanorods prepared by glancing reactive magnetron sputtering. *Mater. Today: Proceed.* 4, 6218–6223 (2017).
26. Y. Sun, C.J. Murphy, K.R. Reyes-Gil, E.A. Reyes-Garcia, J.M. Thornton, N.A. Morris, and D. Raftery, Photoelectrochemical and structural characterization of carbon-doped WO<sub>3</sub> films prepared via spray pyrolysis. *Int. J. Hydrogen Energy* 34(20), 8476–8484 (2009).
27. X.T. Su, F. Xiao, J.L. Lin, J.K. Jian, Y.N. Li, Q.J. Sun, and J.D. Wang, Hydrothermal synthesis of uniform WO<sub>3</sub> microspheres using thiourea as an assistant agent. *Mater. Charact.* 61(8), 831–834 (2010).
28. W. Merchant-Merchan, M.F. Farahani, and Z. Moorhead-Rosenberg, Electron beam induced formation of tungsten sub-oxide nanorods from flame-formed fragments. *Micron* 57, 23–30 (2014).
29. D. Hidayat, A. Purwanto, W.N. Wang, and K. Okuyama, Preparation of size-controlled tungsten oxide nanoparticles and evaluation of their adsorption performance. *Mater. Res. Bull.* 45(2), 165–173 (2010).
30. S. Deki, A.B. Béléké, Y. Kotani, and M. Mizuhata, Synthesis of tungsten oxide thin film by liquid phase deposition. *Mater. Chem. Phys.* 123(2–3), 614–619 (2010).
31. A.A. Ashkarran, M.M. Ahadian, and S.M. Ardakani, Synthesis and photocatalytic activity of WO<sub>3</sub> nanoparticles prepared by the arc discharge method in deionized water. *Nanotechnology* 19(19), 195709 (2008).
32. X.H. Zhu and Q.M. Hang, Microscopical and physical characterization of microwave and microwave-hydrothermal synthesis products. *Micron* 44, 21–44 (2013).
33. F. Güzelçimen, B. Tanören, Ç. Çetinkaya, M.D. Kaya, H.İ Efkere, Y. Özen, and S. Özçelik, The effect of thickness on surface structure of RF sputtered TiO<sub>2</sub> thin films by XPS, SEM/EDS. *AFM and SAM. Vacuum* 182, 109766 (2020).
34. Ç. Çetinkaya, E. Cokduygulular, Y. Özen, I. Candan, B. Kınacı, and S. Özçelik, Determination of surface morphology and electrical properties of MoO<sub>3</sub> layer deposited on GaAs substrate with RF magnetron sputtering. *J. Mater. Sci.: Mater. Electron.* 32(9), 12330–12339 (2021).
35. A.A. Yousif and A.I. Khudadad, Effects of annealing process on the WO<sub>3</sub> thin films prepared by pulsed laser deposition. In IOP Conference Series: Materials Science and Engineering (Vol. 745, No. 1, p. 012064). IOP Publishing (2020).
36. R. Huang, Y. Shen, L. Zhao, and M. Yan, Effect of hydrothermal temperature on structure and photochromic properties of WO<sub>3</sub> powder. *Adv. Powder Technol.* 23(2), 211–214 (2012).
37. R. Rathika, M. Kovendhan, D.P. Joseph, A.S. Kumar, K. Vijayarangamuthu, C. Venkateswaran, K. Asokan, and S.J. Jeyakumar, Effect of 200 MeV Ag<sup>15+</sup> ion beam irradiation at different fluences on WO<sub>3</sub> thin films. *Nucl. Instrum. Methods Phys. Res. Sect. B: Beam Interact. Mater. Atoms* 439, 51–58 (2019).
38. I.P. Jain and G. Agarwal, Ion beam induced surface and interface engineering. *Surf. Sci. Rep.* 66(3–4), 77–172 (2011).
39. V. Kumar, M.K. Jaiswal, R. Gupta, J. Ram, I. Sulania, S. Ojha, and R. Kumar, Effect of low energy (keV) ion irradiation on structural, optical and morphological properties of SnO<sub>2</sub>-TiO<sub>2</sub> nanocomposite thin films. *J. Mater. Sci.: Mater. Electron.* 29(15), 13328–13336 (2018).
40. D.K. Avasthi, Modification and Characterisation of Materials by Swift Heavy Ions. *Def. Sci. J.* 59(4), 401–412 (2009).
41. B. Schattat, W. Bolse, A. Elsanousi, and T. Renz, Interface mixing induced by swift heavy ions at metal-oxide/silicon interfaces. *Nucl. Instrum. Methods Phys. Res., Sect. B* 230(1–4), 240–245 (2005).
42. R.P. Joshi, K. Hareesh, A. Bankar, G. Sanjeev, K. Asokan, D. Kanjilal, and S.D. Dhole, Anti-biofilm activity of Fe heavy ion irradiated polycarbonate. *Nucl. Instrum. Methods Phys. Res., Sect. B* 384, 6–13 (2016).
43. M. Mishra, F. Meinerzhagen, M. Schleberger, D. Kanjilal, and T. Mohanty, Swift heavy ion induced optical and electronic modifications of graphene-TiO<sub>2</sub> nanocomposites. *J. Phys. Chem. C* 119(36), 21270–21277 (2015).
44. B. Bharati, N.C. Mishra, and C. Rath, Effect of 500 keV Ar<sup>2+</sup> ion irradiation on structural and magnetic properties of TiO<sub>2</sub> thin films annealed at 900° C. *Appl. Surf. Sci.* 455, 717–723 (2018).
45. K. Kaviyarasu, P.P. Murmu, J. Kennedy, F.T. Thema, D. Letsholathebe, L. Kotsedi, and M. Maaza, Structural, optical and magnetic investigation of Gd implanted CeO<sub>2</sub> nanocrystals. *Nucl. Instrum. Methods Phys. Res. Sect. B* 409, 147–152 (2017).
46. N.M. Strickland, E.F. Talantsev, N.J. Long, J.A. Xia, S.D. Searle, J. Kennedy, and S. Sathyamurthy, Flux pinning by discontinuous columnar defects in 74 MeV Ag-irradiated YBa<sub>2</sub>Cu<sub>3</sub>O<sub>7</sub> coated conductors. *Physica C* 469(23–24), 2060–2067 (2009).
47. T. Prakash, G.V. Williams, J. Kennedy, and S. Rubanov, Formation of magnetic nanoparticles by low energy dual implantation of Ni and Fe into SiO<sub>2</sub>. *J. Alloy. Compd.* 667, 255–261 (2016).
48. R. Sivakumar, C. Sanjeeviraja, M. Jayachandran, R. Gopalakrishnan, S.N. Sarangi, D. Paramanik, and T. Som, High temperature grown transition metal oxide thin films: tuning physical properties by MeV N<sup>+</sup>-ion bombardment. *J. Phys. D Appl. Phys.* 41(12), 125304 (2008).
49. S. Sharma, A. Paliwal, M. Tomar, F. Singh, N.K. Puri, and V. Gupta, Detailed optical analysis of 100 MeV Ni<sup>7+</sup> ion irradiated WO<sub>3</sub> thin films using surface plasmon resonance. *Radiat. Phys. Chem.* 153, 51–57 (2018).
50. V. Kumar and R. Kumar, Low energy Kr<sup>5+</sup> ion beam engineering in the optical, structural, surface morphological and electrical properties of RF sputtered TiO<sub>2</sub> thin films. *Opt. Mater.* 91(March), 455–469 (2019).
51. J.P. Biersack and L.G. Haggmark, A Monte Carlo computer program for the transport of energetic ions in amorphous targets. *Nucl. Inst. Methods* 174(1–2), 257–269 (1980).

52. M. Miyakawa, K. Ueda, and H. Hosono, Carrier generation in highly oriented WO<sub>3</sub> films by proton or helium implantation. *J. Appl. Phys.* 92(4), 2017–2022 (2002).
53. Y.S. Chaudhary, S.A. Khan, R. Shrivastav, V.R. Satsangi, S. Prakash, D.K. Avasthi, and S. Dass, A study on 170 MeV Au<sup>13+</sup> irradiation induced modifications in structural and photoelectrochemical behavior of nanostructured CuO thin films. *Nucl. Instrum. Methods Phys. Res. Section B Beam Interact. Mater. Atoms* 225(3), 291–296 (2004).
54. G.R. Khan, A. Kandasami, and B.A. Bhat, Augmentation of thermoelectric performance of VO<sub>2</sub> thin films irradiated by 200 MeV Ag<sup>9+</sup>-ions. *Radiat. Phys. Chem.* 123, 55–62 (2016).
55. P. Kumar, P. Sharma, A. Solanki, A. Tripathi, D. Deva, R. Shrivastav, and V.R. Satsangi, Photoelectrochemical generation of hydrogen using 100 MeV Si<sup>8+</sup> ion irradiated electrodeposited iron oxide thin films. *Int. J. Hydrogen Energy* 37(4), 3626–3632 (2012).
56. A. Solanki, J. Shrivastava, S. Upadhyay, V. Sharma, P. Sharma, P. Kumar, and S. Dass, Irradiation-induced modifications and PEC response—a case study of SrTiO<sub>3</sub> thin films irradiated by 120 MeV Ag<sup>9+</sup> ions. *Int. J. Hydrogen Energy* 36(9), 5236–5245 (2011).
57. K. Sarmah, R. Sarma, and H.L. Das, Structural characterization of thermally evaporated CdSe thin films. *Chalcogen. Lett.* 5(8), 153–163 (2008).
58. F. Singh, R.G. Singh, V. Kumar, S.A. Khan, and J.C. Pivin, Softening of phonons by lattice defects and structural strain in heavy ion irradiated nanocrystalline zinc oxide films. *J. Appl. Phys.* 110(8), 083520 (2011).
59. C. Liu, N. Wang, J. Wang, H. Liu, G. Jia, and X. Mu, Modifications in structure and optical property of Cu nanoparticles in SiO<sub>2</sub> by post heavy ion irradiation. *Nucl. Instrum. Methods Phys. Res. Sect. B* 326, 28–32 (2014).
60. A.S. Hassanien and A.A. Akl, Influence of composition on optical and dispersion parameters of thermally evaporated non-crystalline Cd<sub>50</sub>S<sub>50</sub>-xSex thin films. *J. Alloy. Compd.* 648, 280–290 (2015).
61. W. Zhang, Y. Fan, T. Yuan, B. Lu, Y. Liu, Z. Li, G. Li, Z. Cheng, and J. Xu, Ultra-fine tungsten oxide nanowires: synthesis and high selective acetone sensing and mechanism analysis. *ACS Appl. Mater. Interfaces* 12(2020), 3755–3763 (2020).
62. S. Survase, H. Narayan, I. Sulania, and M. Thakurdesai, Swift heavy ion irradiation induced nanograin formation in CdTe thin films. *Nucl. Instrum. Methods Phys. Res., Sect. B* 387, 1–9 (2016).
63. S.K. Srivastava and D.K. Avasthi, Swift heavy ion-induced mixing. *Def. Sci. J.* 59(4), 425 (2009).
64. X. Li, H. Zhu, J. Wei, K. Wang, E. Xu, Z. Li, and D. Wu, Determination of band gaps of self-assembled carbon nanotube films using Tauc/Davis–Mott model. *Appl. Phys. A* 97(2), 341–344 (2009).
65. R. Chauhan, A. Tripathi, and K.K. Srivastava, High-energy ion treatments of amorphous As<sub>40</sub>Se<sub>60</sub> thin films for optical applications. *Progr. Nat. Sci.: Mater. Int.* 24(3), 239–246 (2014).
66. D. Gupta, V. Chauhan, N. Koratkar, F. Singh, A. Kumar, S. Kumar, and R. Kumar, High energy (MeV) ion beam induced modifications in Al<sub>2</sub>O<sub>3</sub>-ZnO multilayers thin films grown by ALD and enhancement in photoluminescence, optical and structural properties. *Vacuum* 192, 110435 (2021).
67. A.S. Hassanien and A.A. Akl, Effect of Se addition on optical and electrical properties of chalcogenide CdS<sub>2</sub> thin films. *Superlattices Microstruct.* 89, 153–169 (2016).
68. A.J. Kronemeijer, V. Pecunia, D. Venkateshvaran, M. Nikolka, A. Sadhanala, J. Moriarty, and H. Sirringhaus, Two-dimensional carrier distribution in top-gate polymer field-effect transistors: correlation between width of density of localized states and Urbach energy. *Adv. Mater.* 26(5), 728–733 (2014).
69. S. Ilican, Y. Caglar, and M. Caglar, Preparation and characterization of ZnO thin films deposited by sol-gel spin coating method. *J. Optoelectron. Adv. Mater.* 10(10), 2578–2583 (2008).
70. S. Ahmad, K. Asokan, and M. Zulfeqar, Investigation of structural and optical properties of 100 MeV F<sup>7+</sup> ion irradiated Ga<sub>10</sub>Se<sub>90-x</sub>Al<sub>x</sub> thin films. *Phil. Mag.* 95(12), 1309–1320 (2015).
71. S.S. Chiad, Optical characterization of NiO doped Fe<sub>2</sub>O<sub>3</sub> thin films prepared by spray pyrolysis. *Method. Int. Lett. Chem. Phys. Astron.* 45, 50–58 (2015).
72. W.W. Yu, L. Qu, W. Guo, and X. Peng, Experimental determination of the extinction coefficient of CdTe, CdSe, and CdS nanocrystals. *Chem. Mater.* 15(14), 2854–2860 (2003).
73. J. Liqiang, Q. Yichun, W. Baiqi, L. Shudan, J. Baojiang, Y. Libin, and S. Jiazhong, Review of photoluminescence performance of nano-sized semiconductor materials and its relationships with photocatalytic activity. *Sol. Energy Mater. Sol. Cells* 90(12), 1773–1787 (2006).
74. C.P. Saini, A. Barman, D. Banerjee, O. Grynko, S. Prucnal, M. Gupta, and A. Kanjilal, Impact of self-trapped excitons on blue photoluminescence in TiO<sub>2</sub> nanorods on chemically etched Si pyramids. *J. Phys. Chem. C* 121(21), 11448–11454 (2017).
75. D. Wojcieszak, M. Mazur, D. Kaczmarek, J. Morgiel, G. Zatoryb, J. Domaradzki, and J. Misiewicz, Influence of Nd dopant amount on microstructure and photoluminescence of TiO<sub>2</sub>: Nd thin films. *Opt. Mater.* 48, 172–178 (2015).
76. F. Wang, C. Di Valentin, and G. Pacchioni, Semiconductor-to-metal transition in WO<sub>3-x</sub>: Nature of the oxygen vacancy. *Phys. Rev. B* 84(7), 073103 (2011).
77. H.J. Nam, T. Sasaki, and N. Koshizaki, Optical CO gas sensor using a cobalt oxide thin film prepared by pulsed laser deposition under various argon pressures. *J. Phys. Chem. B* 110(46), 23081–23084 (2006).
78. K.R. Nagabhushana, B.N. Lakshminarasappa, G.T. Chandrappa, D. Haranath, and F. Singh, Swift heavy ion induced photoluminescence studies in aluminum oxide. *Radiat. Eff. Defects Solids* 162(5), 325–332 (2007).
79. S. Chandramohan, R. Sathyamoorthy, P. Sudhagar, D. Kanjilal, D. Kabiraj, and K. Asokan, Swift heavy ion beam irradiation induced modifications in structural, morphological and optical properties of CdS thin films. *Nucl. Instrum. Methods Phys. Res., Sect. B* 254(2), 236–242 (2007).
80. M.K. Jaiswal and R. Kumar, Studies of dense electronic excitation induced modification in cobalt doped SnO<sub>2</sub> thin films prepared by RF sputtering technique. *J. Alloy. Compd.* 648, 550–558 (2015).
81. K.R. Nagabhushana, B.N. Lakshminarasappa, C. Pandurangappa, I. Sulania, P.K. Kulria, and F. Singh, Ion beam induced modifications in electron beam evaporated aluminum oxide thin films. *Nucl. Instrum. Methods Phys. Res. Sect. B: Beam Interact. Mater. Atoms* 266(8), 1475–1479 (2008).
82. M.K. Jaiswal, D. Kanjilal, and R. Kumar, Swift heavy ion induced modification in morphological and physico-chemical properties of tin oxide nanocomposites. *Nucl. Instrum. Methods Phys. Res., Sect. B* 315, 179–183 (2013).
83. J.C. Liu, J. Li, and J.W. Mayer, Temperature effect on ion-irradiation-induced grain growth in Cu thin films. *J. Appl. Phys.* 67(5), 2354–2358 (1990).
84. P. Pineda-Domínguez, M. Ramos, J. Nogan, O.A. López-Galán, J.L. Enríquez-Carrejo, T. Boll, and M. Heilmair, Piezoelectric response in WO<sub>3-x</sub> thin films by aluminum clustering. *Res. Sq.* (2021). <https://doi.org/10.21203/rs.3.rs-384370/v1>.
85. P.K. Kuirí and J. Ghatak, Ion irradiation induced amorphization of SnO<sub>2</sub> nanoparticles embedded in SiO<sub>2</sub>. *Vacuum* 85(2), 135–138 (2010).
86. S.K. Gautam, A. Chettah, R.G. Singh, S. Ojha, and F. Singh, Swift heavy ion irradiation induced phase transformation in undoped and niobium doped titanium dioxide composite thin films. *Nucl. Instrum. Methods Phys. Res., Sect. B* 379, 224–229 (2016).

87. M.A. Arvizu, H.Y. Qu, U. Cindemir, Z. Qiu, E.A. Rojas-González, D. Primetzhofer, and G.A. Niklasson, Electrochromic  $\text{WO}_3$  thin films attain unprecedented durability by potentiostatic pretreatment. *J. Mater. Chem. A* 7(6), 2908–2918 (2019).
88. T.H. Fleisch and G.J. Mains, An XPS study of the UV reduction and photochromism of  $\text{MoO}_3$  and  $\text{WO}_3$ . *J. Chem. Phys.* 76(2), 780–786 (1982).
89. X. Zheng, F. Ren, S. Zhang, X. Zhang, H. Wu, X. Zhang, and C. Jiang, A general method for large-scale fabrication of semi-conducting oxides with high SERS sensitivity. *ACS Appl. Mater. Interfaces.* 9(16), 14534–14544 (2017).
90. X. Xiang, Z. He, J. Rao, Z. Fan, X. Wang, and Y. Chen, Applications of Ion Beam Irradiation in multifunctional oxide thin films: a review. *ACS Appl. Electron. Mater.* 3(3), 1031–1042 (2021).
91. X. Chu, T. Chen, W. Zhang, B. Zheng, and H. Shui, Investigation on formaldehyde gas sensor with ZnO thick film prepared through microwave heating method. *Sens. Actuators, B Chem.* 142(1), 49–54 (2009).
92. Y. Zhen, J. Zhang, W. Wang, Y. Li, X. Gao, H. Xue et al., Embedded  $\text{SnO}_2$ /Diatomaceous earth composites for fast humidity sensing and controlling properties. *Sens. Actuat. B: Chem.* 303, 127137 (2020).
93. P. Dhivya, A.K. Prasad, and M. Sridharan, Nanostructured  $\text{TiO}_2$  films: enhanced  $\text{NH}_3$  detection at room temperature. *Ceram. Int.* 40(1), 409–415 (2014).
94. T.T. Nguyen, H.N. Choi, M.J. Ahemad, D. Van Dao, I.H. Lee, and Y.T. Yu, Hydrothermal synthesis of  $\text{In}_2\text{O}_3$  nanocubes for highly responsive and selective ethanol gas sensing. *J. Alloy. Compd.* 820, 153133 (2020).
95. A.M. Ruiz, G. Sakai, A. Cornet, K. Shimanoe, J.R. Morante, and N. Yamazoe, Cr-doped  $\text{TiO}_2$  gas sensor for exhaust  $\text{NO}_2$  monitoring. *Sens. Actuators, B Chem.* 93(1–3), 509–518 (2003).
96. J.F. Fernández-Sánchez, T. Roth, R. Cannas, M.K. Nazeeruddin, S. Spichiger, M. Grätzel, and U. Spichiger-Keller, E, Novel oxygen sensitive complexes for optical oxygen sensing. *Talanta* 71(1), 242–250 (2007).
97. M.V. Vaishampayan, R.G. Deshmukh, and I.S. Mulla, Influence of Pd doping on morphology and LPG response of  $\text{SnO}_2$ . *Sens. Actuators, B Chem.* 131(2), 665–672 (2008).
98. O.M. Slobodian, Y.V. Gomeniuk, A.V. Vasin, A.V. Rusavsky, P.N. Okholin, O.Y. Gudymenko, and A.N. Nazarov, Graphitic nanoporous carbon thin films: fabrication method, structural, electrical and gas sensor properties. *ECS Trans.* 97(5), 151 (2020).

**Publisher's Note** Springer Nature remains neutral with regard to jurisdictional claims in published maps and institutional affiliations.

Springer Nature or its licensor (e.g. a society or other partner) holds exclusive rights to this article under a publishing agreement with the author(s) or other rightsholder(s); author self-archiving of the accepted manuscript version of this article is solely governed by the terms of such publishing agreement and applicable law.